

A Thermo-Fluidic Model for a Low Power Xenon Resistojet

*Presented at Joint Conference of 30th International Symposium on Space Technology and Science,
34th International Electric Propulsion Conference and 6th Nano-satellite Symposium
Hyogo-Kobe, Japan
July 4–10, 2015*

Federico Romei* and Angelo N. Grubišić†
University of Southampton, Southampton, SO17 1BJ, UK

Dave Gibbon‡ and Oliver Lane§
Surrey Satellite Technology Ltd, Guildford, GU2 7YE, UK

Rémi A. Herfort¶
École Supérieure des Techniques Aéronautiques et de Construction Automobile, Paris, 92532, France

and

Graham T. Roberts ||
University of Southampton, Southampton, SO17 1BJ, UK

A next generation high performance xenon resistojet delivering specific impulse above 90s would be of significant benefit to both small and newer all-electric spacecraft. Such performance would require a xenon propellant temperature of > 3000 K for gas dynamic expansion. Operation at such extreme temperatures and power densities requires a detailed understanding of numerous physical processes in order to converge on a workable design. The highly interdependent nature of these processes, such as resistive dissipation, heat transfer, fluid dynamics and material stress, means that studying each of them discreetly only provides limited insight. This paper thus presents a validated coupled multiphysics model of the conventional SSTL-T50 thruster. The paper shows the preliminary results of a model for the T-50 nozzle and implements the compressible Navier-Stokes equation coupled with conductive, radiative and convective heat transfer in both solid and fluid. The CFD multiphysics model is coupled with an optimization solver, in order to converge on experimental data for the thruster. The calculated results of this nozzle are presented as centerline variations of Mach number and static temperature, with an analysis of nozzle exit profiles of Mach number and including radiation loss from the nozzle.

*PhD Candidate, Aeronautics, Astronautics and Computational Engineering, F.Romei@soton.ac.uk.

†Lecturer, Aeronautics, Astronautics and Computational Engineering, A.Grubic@soton.ac.uk.

‡Propulsion Expert, D.Gibbon@SSTL.co.uk.

§Propulsion Team Leader, O.Lane@sstl.co.uk

¶Postgraduate Student, Remi.Herfort@estaca.eu

||Senior Lecturer, G.T.Roberts@soton.ac.uk

Nomenclature

S/C	= Spacecraft
F	= Thrust
I_{sp}	= Specific Impulse
\dot{m}	= Mass flow rate
T_{BG}, p_{BG}	= Back-ground temperature (assumption) and pressure (experimental) of the vacuum chamber
T_s, p_s	= Experimental values of supply temperature and pressure
T_{in}, p_{in}	= Computational nozzle inlet temperature and pressure
p_{out}	= Total pressure at the exit section of the nozzle
T_N	= Temperature measured experimentally at the outer surface of the nozzle
T_{nozzle}	= Computational average temperature of the nozzle inlet section wall
A_{in}	= Nozzle inlet area
α	= Nozzle divergent half-angle
\mathbf{u}	= Velocity vector
z, w	= Axial space component and velocity
r, u	= Radial space component and velocity
ρ	= Density
Re	= Reynolds number
μ	= Dynamic viscosity
C_p	= Specific heat at constant pressure
γ	= Ratio of specific heats
k	= Thermal conductivity
\mathbf{F}	= Volume force vector
Q_{vh}	= Viscous heat
W_p	= Pressure work
ϵ	= Surface emissivity
σ	= Stefan-Boltzmann constant
R	= Xenon gas constant
$RANS$	= Reynolds-Averaged Navier-Stokes equations
I_T	= Turbulence intensity
L_T	= Turbulence length scale
M	= Mach number
J	= Objective function of the optimization solver
g_0	= Acceleration of gravity
P_{tot}	= Total input power
P_{heat}	= Power associated to the gas heating process
P_e	= Input electrical power
P_0	= Gas power at the initial cold temperature
η_{heat}	= Heat exchanger gas heating efficiency

I. Introduction

THE SSTL T-50 resistojet thruster shown in Fig.1, has been the basis of SSTL hot gas propulsion systems since 2002. There are 29 thrusters in orbit on 20 spacecraft, with a further 6 thrusters awaiting launch. The initial application was with butane propellant on Alsat-1 and it has since been used in a further 11 butane systems including ESAs Giove-A (Table 2). The thruster is also used as part of xenon propulsion systems, including ESAs Proba-2, RapidEye constellation (Fig.1) and DMC3. The variants of the thruster are detailed in Table 1.



Figure 1. T50 Resistojet (left) Rapid Eye Constellation Satellites 1-5 (right)

Table 1. The variants of SSTLs low cost resistojet

Variant	Redundant heater power	Propellant	Thrusters	Typical operation temperature	I_{sp}
T50	50W	Xe, N ₂ , Butane	Qualification Model only	Up to 650°C	Up to 57 s
T30	30W	Xe	10 launched on 10 S/Cs, 2 waiting launch	530°C	48 sec
T15	15W	Butane	19 launched on 10 S/Cs, 4 waiting launch	250 - 350°C	> 100 s

The variants are physically identical, with the only difference being the thruster operating power. The T-50 is 60mm long by 20mm diameter, weighs 50grams and is manufactured using two Inconel coaxial sheathed heaters wound on a central bobbin. Propellant enters the back of the thruster and is forced to spiral around the heater, hence increasing the dwell time within the heat exchanger. The heater power is rated at an input voltage of 28Vdc and the thruster is designed to run directly off the spacecraft 28Vdc bus, hence no additional control electronics is required for operation.

II. Nozzle Study

Figure 2 (right) shows the T50 test set-up from thruster performance testing at the ESA Electric Propulsion Laboratory. The xenon supply to the thruster is pressure regulated with mass flow rate measured via a mass flow rate sensor. A pressure transducer measures the supply pressure upstream of the thruster's heat exchanger. From thruster tests, the pressure drop across the heat exchanger is considered negligible.

The measured experimental parameters were: propellant mass flow rate, \dot{m} ; supply pressure, p_s ; background pressure, p_{BG} ; thruster nozzle temperature, T_N ; supply temperature, T_s , and thrust, F^1 .

The thruster nozzle temperature, is measured with a k-type thermocouple secured to the exterior of the nozzle (Fig.2, left). The gas temperature inside the nozzle was not directly measured in these tests, however

Table 2. SSTL resistojets missions

Mission	Launch	Propellant	Number of thruster
Alsat-1	2002	Butane	1
NigeriaSat-1	2003	Butane	1
UK-DMC-1	2003	Butane	1
Bilsat-1	2003	Butane	1
Beijing-1	2005	Xenon	1
Giove-A	2005	Butane	10
Rapideye FM1 to FM5	2008	Xenon	5
UK-DMC-2	2009	Butane	1
Deimos-1	2009	Butane	1
SumbandilaSat	2009	Butane	1
Proba 2	2009	Xenon	1
NigeriaSat-X	2011	Butane	1
NigeriaSat-2	2011	Xenon	1
Exactview-1	2012	Butane	1
KazEOSat-2	2014	Xenon	1
TechDemoSat-1	2014	Xenon	1
DMC3 FM1 to FM3	2015	Xenon	3
Alsat-1b	2016	Butane	1
NovaSAR-1	2016	Xenon	1
KazSTSAT	2016	Butane	1

it has been estimated in previous experiments for Butane propellant. These estimations were made with a supply pressure of 2 bar, from a pressure measurement on the pressure-tap shown in the blank-off in Fig.2 (left). In this case the nozzle inlet gas temperature, T_{in} , was found to be slightly higher than the nozzle temperature, T_N . For example, with a nozzle temperature of 500 K, the inlet gas temperature was found to be 516 K.

The current study couples CFD and parameter optimization to trim the thruster nozzle temperature T_N , and the inlet pressure p_{in} , to match experimental data in order to estimate the inlet gas temperature and pressure prior to entry into the nozzle. Mach number and velocity profiles along the axial centerline, including throughout the nozzle can then be analyzed.

A. Nozzle Geometry

The T50 resistojet contains a 14-deg half-angle conical nozzle, made of 316 grade stainless steel. The throat to nozzle exit area ratio corresponds to 211, while the throat to inlet area ratio is 661. The throat diameter is 0.42 mm and the nozzle wall thickness of the diverging section is 1 mm. For the CFD simulations, the selected radius of curvature upstream and downstream of the throat have the same dimension of the throat radius and diameter respectively. The throat is located at $z = 6.10$ mm, and the total length of the nozzle is 17.80 mm (Fig.5 at page 7).

The available experimental data corresponds to 24 different cases, which are the combinations of different inlet pressure and temperature conditions, corresponding to the power applied to the resistojet heaters. Table 3 shows the throat Reynolds number, Re_t , evaluated from Eq.(1)

$$Re_t = \frac{\rho_t w_t d_t}{\mu_t} = \frac{4\dot{m}_t}{\pi \mu_t d_t} \quad (1)$$

Re_t has been calculated with the right-hand side of the equation, using the experimental xenon mass flow rate, and the dynamic viscosity, which is evaluated from the interpolation of experimental data found

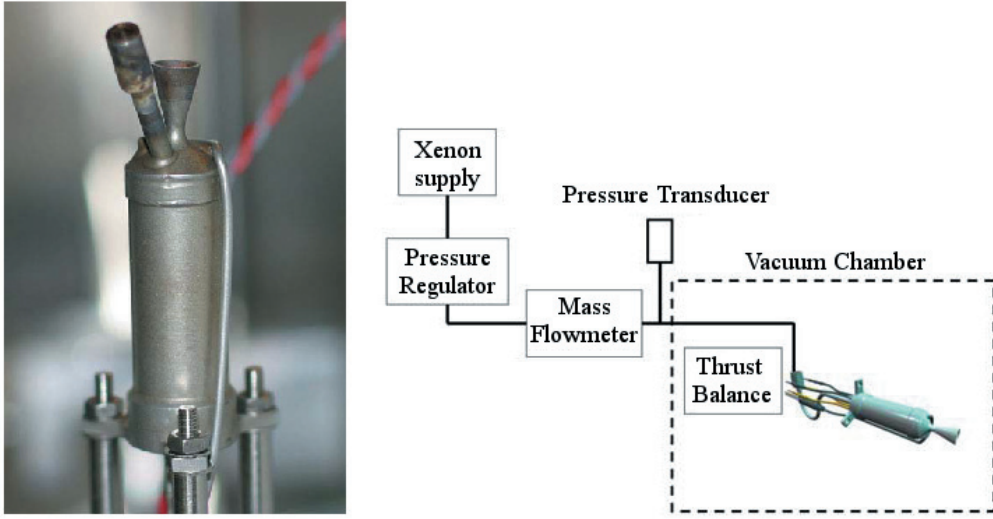


Figure 2. SSSL-T50 resistojet mounted vertically on a thrust balance (left) and test set-up for performance measurement (right) at the European Space Agency Electric Propulsion Laboratory



Figure 3. Assembly view with transparent thruster housing showing coaxial heating elements

in literature³, where it is assumed $T_{in} = T_N$. Hence, for the CFD simulations, the cases (65 W, 1 bar), (50 W, 1 bar), (40 W, 1 bar), (30 W, 1 bar), and (20 W, 1 bar), will be solved using the laminar flow equations. For the remaining cases, the Reynolds-Averaged Navier-Stokes equations, RANS, are used to model the flow.

B. Multiphysics Model

COMSOL Multiphysics^{®7} has been adopted to solve the problem as it allows fully coupled multi-physics modelling and it includes several optimization tools. The thermo-fluidic model of the T50 nozzle is axial-symmetric and stationary, and uses the High Mach Number Flow interface which models a gas flow at low or moderate Reynolds number in the compressible case and can model both laminar and turbulent flow. The compressible Navier-Stokes equations in the vectorial form are: conservation of momentum (2a), mass (2b) and energy (2c). In addition the interface Heat Transfer in Solids, is used to model the nozzle wall heat transfer conductively and radiatively including both surface to surface and surface to ambient radiation:

Table 3. Reynolds number calculated at the nozzle throat

P_e, W	1 bar	2 bar	3 bar	4 bar
65	1906	4283	6845	9450
50	2094	4735	7434	10292
40	2363	4968	7967	11154
30	2557	5375	8546	12158
20	2879	6307	10215	14091
10	5563	9582	15180	20926

$$\rho(\mathbf{u} \cdot \nabla) \mathbf{u} = \nabla \cdot \left[-p\mathbf{I} + \mu(\nabla \mathbf{u} + (\nabla \mathbf{u})^T) - 2/3\mu(\nabla \cdot \mathbf{u})\mathbf{I} \right] + \mathbf{F} \quad (2a)$$

$$\nabla \cdot (\rho \cdot \mathbf{u}) = 0 \quad (2b)$$

$$\rho C_p(\mathbf{u} \cdot \nabla) T = \nabla \cdot (k\nabla T) + Q + Q_{vh} + W_p \quad (2c)$$

where Q_{vh} is the viscous heat, W_p is the pressure work, Q contains the heat source, and F is the volume force (here $Q = 0$ and $F = 0$). Heat Transfer in Solids is applied on the solid nozzle domain, where the conductive term of Eq.2c is applied. For the turbulence case, the standard $k - \epsilon$ model is used, with the built-in Kays-Crawford heat transport turbulence model⁷.

For the Xenon gas, both thermal conductivity, k_{Xe} , and dynamic viscosity, μ_{Xe} (Fig.4), are evaluated as cubic spline interpolations from a set of experimental data points given by Bich et al.³. These interpolations were found to give a better final result on the simulations with respect to the built-in polynomial functions of temperature. Accurate material properties were applied for the 316 grade stainless steel nozzle, with the thermal conductivity approximated as a linear function of the temperature.

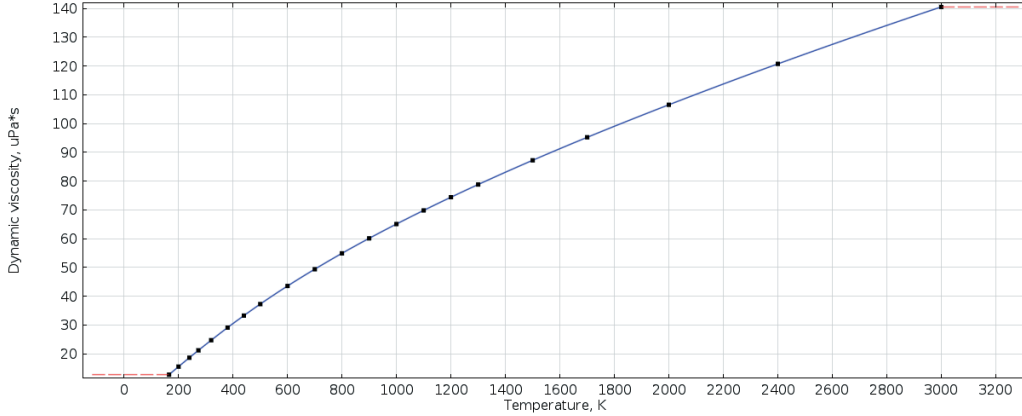


Figure 4. Xenon dynamic viscosity, μPa

1. Mesh Optimization

The mesh selected for the nozzle is structured for the Xenon gas domain, while it is unstructured for the solid part of the nozzle (Fig.5), where only the heat transfer equation is solved. The structured grid is made of a proportional number of axial elements with respect to the number of radial elements. In the converging and diverging parts of the nozzle, the grid axial spacing evolves to maintain a nearly constant aspect ratio.

The solution accuracy has been studied in a convergence study by varying the number of radial elements. Figure 6 shows how the numerical solution of the model approaches an asymptote as the number of radial elements increases. However, a trade-off between the solution accuracy and the computational time led to

select 40 radial elements as an acceptable value, since the model error is less than 1%. The resulting Xenon gas-domain computational grid has the size 40×200 .

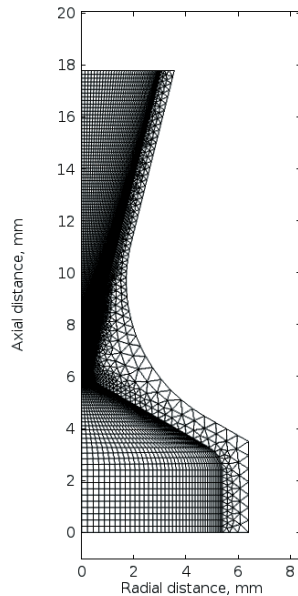


Figure 5. Computational grid for the T50 nozzle

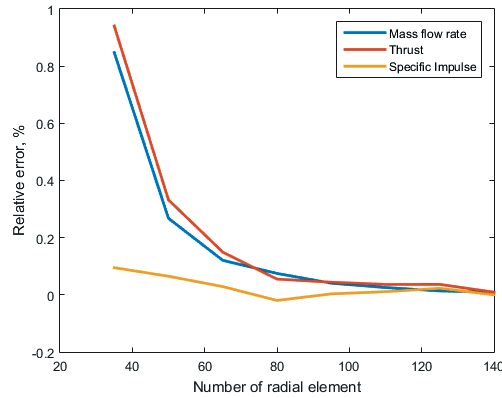


Figure 6. Mesh solution accuracy

2. Supercomputing Cluster

Computations were performed on the University of Southampton Iridis supercomputer cluster (Fig.7). The current Iridis 4 is our fourth generation cluster and is one of the largest computational facilities in the UK. Its performance characteristics area as follows:

- 750 compute nodes with dual 2.6 GHz Intel Sandybridge processors;
- Each compute node has 16 CPUs per node with 64 GB of memory;
- 4 high-memory nodes with two 32 cores and 256 GB of RAM;
- 24 Intel Xeon Phi Accelerators;
- 3 login nodes with 16 cores and 125 GB of memory;
- In total 12320 processor-cores providing 250 TFlops peak;
- 1.04 PB of raw storage with Parallel File System;
- InfiniBand network for interprocess communication;
- Moab HPC Suite - advanced workload management system from Adaptive Computing;

Initial studies were conducted using a i7 Intel workstation with 32GB of RAM. While this was sufficient for preliminary studies, for the coupled CFD and optimization simulations the computational time became excessive because of the many iterations involved in the optimization process. With the IRIDIS supercomputing cluster, it was possible to use between 2 and 4 nodes to compute in parallel the iterations of the parametric sweep used by the solver. Typically for the laminar flow simulations the computational time was 20 minutes, while for the turbulent flow cases it took about one hour for each one of the 24 cases.

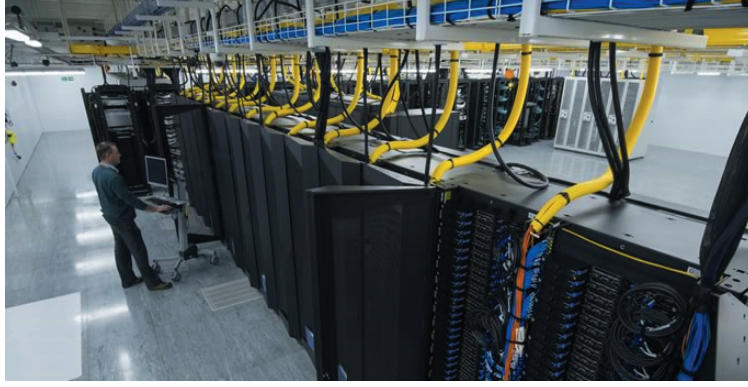


Figure 7. University of Southampton Iridis supercomputer cluster

3. Boundary Conditions

For the laminar flow no-slip condition, Eq.3a, is applied on the nozzle internal wall, whereas for the turbulence model, the wall functions do apply. The study includes the surface-to-ambient radiation applied on the outer nozzle wall, modelled by Eq.3b, where k is the Stainless Steel thermal conductivity, $\epsilon = 0.6$ the surface emissivity (assumption), and $\sigma = 5.6703 \times 10^{-8} W/(m^2K^4)$ is the Stefan-Boltzmann constant. On the inner boundaries of the converging part of the nozzle, surface-to-surface radiation is applied using the built-in Hemicube method to calculate the view factors.

On the assumption that the inlet gas temperature and the inlet nozzle section are not at the same temperature in equilibrium conditions, a temperature boundary condition is applied to the inlet nozzle wall, its notation is T_{nozzle} .

The inlet condition for the gas is specified in terms of total pressure, total temperature and Mach number. The inlet Mach number, M_0 , is evaluated using the equation for an ideal compressible gas, in the assumption of isentropic flow. Eq.3c is used, where $A_{in} = 91.6 mm^2$ is the nozzle inlet area, p_t is the inlet total pressure (assuming $p_t = p_s$), $\gamma = 1.67$ is the ratio of specific heats of Xe, $R = 63.5 J/(kgK)$ is the Xe gas constant, T_t is the inlet total temperature (assuming $T_t = T_N$). For the turbulence model, the inlet parameters of turbulent intensity, I_T , and turbulence length scale, L_T , are calculated using the equation for a fully developed pipe flow, Eq.3d and 3e respectively. $L_T = 0.41 mm$, while I_T assumes different values depending on the corresponding inlet Reynolds number, Re_{in} .

The outlet condition of the flow is set as static pressure equal to the experimental background pressure of the vacuum chamber, p_{BG} . It is assumed that the background temperature of the vacuum chamber is near room temperature at $T_{BG} = 300 K$.

$$\mathbf{u}_{wall} = 0 \quad (3a)$$

$$\mathbf{n} \cdot (-k\nabla T) = \epsilon\sigma(T^4 - T_{BG}^4) \quad (3b)$$

$$\dot{m} = \frac{Ap_t}{\sqrt{T_t}} \sqrt{\frac{\gamma}{R}} M \left(1 + \frac{\gamma-1}{2} M^2\right)^{-\frac{\gamma+1}{2(\gamma-1)}} \quad (3c)$$

$$I_T = 0.16Re_{in} \quad (3d)$$

$$L_T = 0.038d_h \quad (3e)$$

4. Optimization Solver

The built-in Nelder-Mead optimization solver has been used to minimize the objective function, J , which is defined as:

$$J = (I_{sp} - \hat{I}_{sp})^2 + (F - \hat{F})^2 \times 10^6 + (T_N - \hat{T}_N)^2 \quad (4)$$

$$I_{sp} = F/(\dot{m}g_0) \quad (5a)$$

$$F = 2\pi \int_0^r [\rho w^2 + (p - p_{BG})]rdr \quad (5b)$$

$$\dot{m} = 2\pi \int_0^r \rho wrdr \quad (5c)$$

where the terms marked with a hat, are the experimental values of specific impulse, thrust and thermo-couple temperature respectively. Equations 5a, 5b and 5c show the definitions of specific impulse, thrust and mass flow rate respectively, defined on the nozzle exit boundary. $g_0 = 9.80665 \text{ m/s}^2$ is the acceleration of gravity. The solver finds the minimum of the the objective function J , given the control variables selected: p_{in} , T_{in} and T_{nozzle} . In order to ask the same accuracy on the three objective function terms, a weight is necessary on the thrust expression. The optimality tolerance has been fixed to 0.01, meaning that the optimization solver stops iterating when the objective function satisfies $J \leq 0.01$.

The parameters have been selected since they are coupled principally with a single objective function term. In particular, from the physics point of view, I_{sp} is mainly dependent on T_{in} , F is mainly dependent on p_{in} , and T_N is mainly dependent on T_{nozzle} . The convergence of the optimization solver to the selected optimality tolerance, depends strongly on the initial conditions given. With trial and error, and the knowledge of the nozzle physics, satisfactory initial conditions were found.

Table 4. Example of optimization solver iterations (65W, 1bar)

step	p_{in}	T_{in}	T_{nozzle}	T_N	F	I_{sp}	\dot{m}	J
-	Pa	K	K	K	mN	s	mg/s	-
1	113985	1082.250	883.173	858.277	21.138	52.861	40.776	2.390
2	107985	1082.250	883.173	858.239	19.906	52.629	38.568	1.927
3	113985	1172.250	883.173	866.668	21.065	54.100	39.706	76.066
4	113985	1082.250	913.173	882.654	21.094	53.092	40.515	609.579
5	109985	1142.250	853.173	839.179	20.314	53.302	38.863	354.716
61	109107	1188.671	870.457	858.044	20.069	54.009	37.892	4.300E-03
62	109270	1184.804	870.899	857.990	20.105	53.969	37.987	2.560E-04
63	109337	1185.652	870.855	858.046	20.118	53.983	38.003	2.180E-03
64	109207	1185.794	870.775	857.994	20.092	53.979	37.956	3.278E-04
65	109270	1184.804	870.899	857.990	20.105	53.969	37.987	2.560E-04

C. Results and Discussion

The optimization study was made for the 24 experimental cases. The main outputs of the simulation are the space solutions of: mass flow rate; temperature; Mach number; nozzle radiation loss. Table 4 shows an example of the CFD-optimization iterations. The initial values of inlet pressure and temperature have been estimated by optimization through trial and error.

The mass flow rate, \dot{m} , can be used as a model validation parameter. Table 5 shows the percentage relative error of the mass flow rate with respect to the experimental values. In the worst case (65 W, 1 bar), the 3.3% of relative error on \dot{m} is considered an acceptable value. As a further check on the numerical solution accuracy, the global mass flow rate conservation has been compared in several axial sections along the nozzle length. The mass flow rate error is found to be about 0.5% from those measured in experiments, which is considered adequate as an engineering estimate.

Table 6 shows the solution for the nozzle inlet total temperature. This temperature can also considered an estimate of the outlet heat exchanger gas temperature, as they are coincident in a fully assembled thruster. Figure 8 shows the correlation between the measured temperature at the surface of the nozzle, T_N , and the hot gas entering the nozzle temperature, T_{in} . Some conclusions on the thruster heat exchanger are

Table 5. Mass flow rate relative error, %

P_e , W	1 bar	2 bar	3 bar	4 bar
65	3.262	2.278	1.475	-0.103
50	-1.491	0.068	-0.014	0.002
40	-3.696	0.050	0.027	-0.017
30	-2.153	0.462	0.167	0.254
20	-0.157	-0.536	0.228	0.306
10	-0.532	-0.223	-0.244	-0.052

deducted from the calculated inlet temperature of the nozzle. The T50 heat exchanger efficiency, η_{heat} , can be defined as P_{heat}/P_{tot} , where $P_{heat} = \dot{m}c_p\Delta T$ is the power required to heat the gas from the initial to the final temperature, $P_{tot} = P_{el} + P_0$, is the sum of the electrical input power and the inlet gas power, at the initial temperature $T_0 = 300 K$. From experiments, η_{heat} , is found to improve with chamber pressure. However, since mass flow rate is proportional to the inlet pressure, even if the heating efficiency improves with pressure, the final gas temperature, T_{in} , for higher pressure cases remains lower.

Table 7 shows the simulation results on the radiation loss from the nozzle outer surface to the ambient. These results are calculated using Eq.3b in the assumption of $\epsilon = 0.6$. It is evident that the radiation power is proportional to the fourth power of the nozzle surface temperature, as a result the maximum radiated power corresponds to the 65 W cases.

Considering the case with a power input of 30 W, Fig.10 shows the axial variation of the centerline Mach number. It is evident that the 1 bar laminar flow solution provides the lowest exit Mach number among the four cases considered. This is also shown in Fig.11, where the Mach profiles are compared in the exit section of the nozzle. It is clear that a wider portion of the exit radius is subsonic, with the subsonic depth reaching about 2.27 mm into the flow field. For this reason, the nozzle area ratio results reduced, leading to lower expansion of the gas. The static temperature profiles are shown in Figures 12 and 13. Due to the lower level of expansion, the static temperatures for the 1 bar laminar case result to be higher both at the nozzle exit and the nozzle centerline.

The Mach number is a non-zero value at the wall for the other cases, where the RANS equations have been used since the *wall functions* have been implemented as boundary condition. Wall functions assume that the viscous boundary layer has zero-thickness, and the computational wall velocity corresponds to a non-zero analytical solution. This technique is used to save considerably the computational cost.

Figure 9 shows the T50 nozzle temperature and Mach number solutions plotted in three dimensions, for the 30 W case at 1 bar inlet pressure. The temperatures, for both the gas and the solid wall, are shown in four solution slices for the convergent section of the nozzle. The first slice at the bottom, shows the constant temperature conditions for the nozzle inlet wall section, $T_N = 741 K$, and for the xenon gas, $T_{in} = 947 K$. From the Mach number iso-surface profiles at the diverging section, it can be seen that the subsonic portion of the flow at the nozzle exit plane cannot be considered negligible.

Table 6. Average inlet static temperature, K

P_e , W	1 bar	2 bar	3 bar	4 bar
65	1185	943	864	809
50	1065	870	791	733
40	996	859	797	724
30	947	800	734	676
20	732	650	580	557
10	492	508	472	483

Table 7. Estimated nozzle radiation-to-ambient loss, W

P_e , W	1 bar	2 bar	3 bar	4 bar
65	7.5	7.6	7.5	7.3
50	6.2	6.2	6.0	5.7
40	4.9	4.8	4.9	4.5
30	4.0	4.1	3.9	3.6
20	2.6	2.6	2.4	2.3
10	0.3	0.7	0.7	0.7

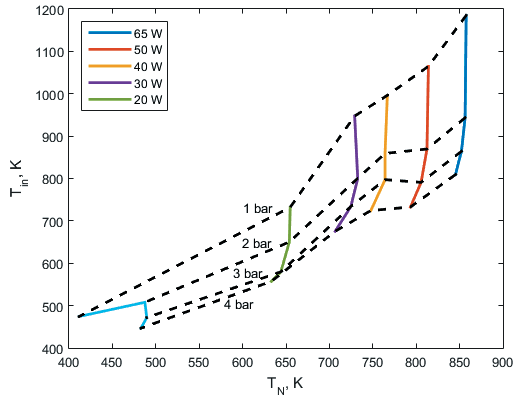


Figure 8. Correlation between nozzle temperature T_N (from experiment) and inlet gas temperature T_{in} (simulation output) for various power levels and supply pressures of the T50 thruster with Xenon propellant

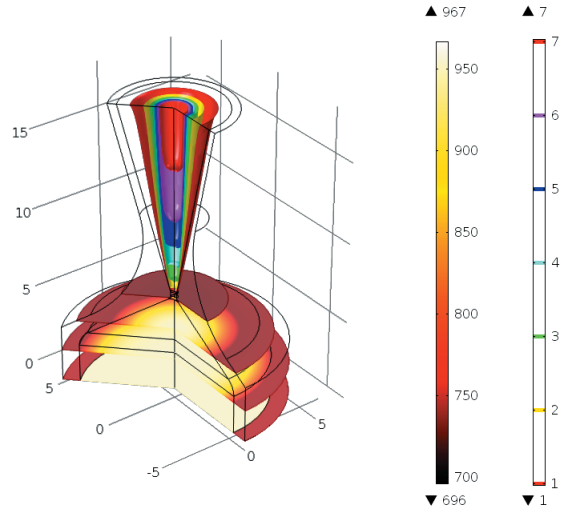


Figure 9. Static temperature in K (for the converging section) and Mach number iso-surface profiles (for the diverging section) for the 30W case at 1 bar inlet pressure

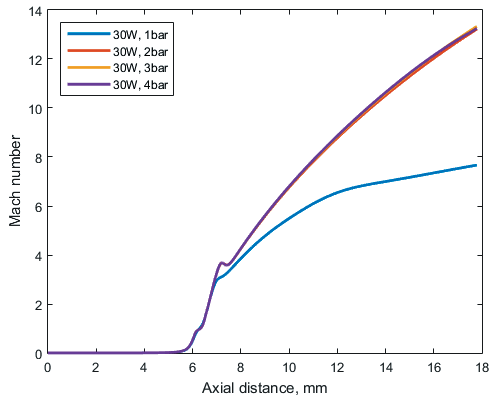


Figure 10. Axial variations of centerline Mach number, nozzle throat located at 6.1 mm downstream, nozzle exit plane located at 17.8 mm

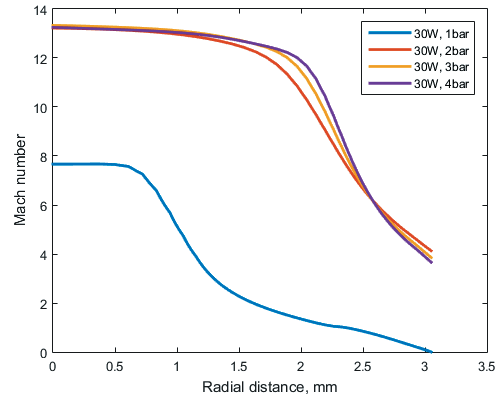


Figure 11. Mach number profiles at the nozzle exit plane in the 30W operative condition at a range of inlet pressures between 1 and 4 bar, plot shows radial distance from the nozzle centerline

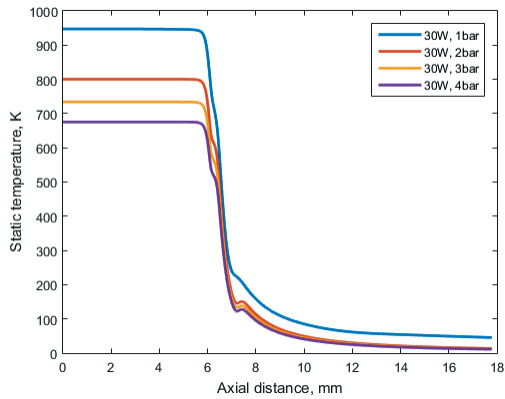


Figure 12. Axial variations of centerline static temperature, nozzle throat located at 6.1 mm downstream, nozzle exit plane located at 17.8 mm

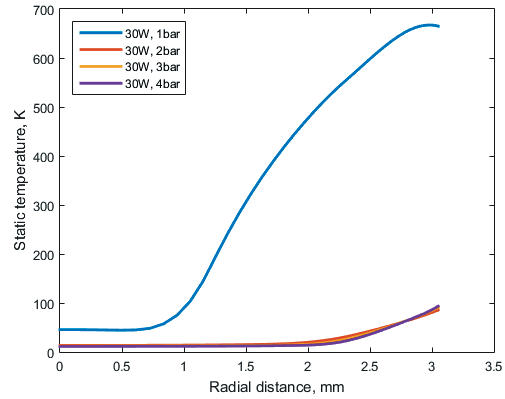


Figure 13. Exit static temperature profiles at the nozzle exit plane in the 30W operative condition at a range of inlet pressures between 1 and 4 bar, plot shows radial distance from the nozzle centerline

1. Nozzle Optimization

As a part of this study, further analysis was conducted on whether the divergence angle of SSTL T-50 resistojets could be further optimized. Since the resistojets are designed to operate at low chamber pressure, on the order of 1 bar, with thrust levels on the order of 100mN, they require small throat dimensions. As a consequence, the resulting throat Reynolds number is low, leading to significant viscous losses on the nozzle diverging wall. As a result, a trade-off is necessary between viscous losses and divergence loss. The CFD-optimization coupling, allows an accurate estimate on the optimum nozzle geometry capable to maximize the thrust, hence I_{sp}^5 .

The T50 Xenon resistojets operate at a wide range of pressures, resulting in most cases to be characterized by turbulent flow as been previously demonstrated. The turbulent boundary layer, has a typical dimension of 1% of the free-stream flow region. As a consequence, the resulting Mach number at the nozzle exit, can be considered entirely supersonic. Therefore, in the turbulent flow cases, the viscous losses are negligible in comparison with the divergence losses. For the laminar flow regime instead, a large subsonic region exists at the exit of the nozzle, extending approximately 10% into the radius of the nozzle. Among the 24 cases, the one with the lowest Re_t (65 W of power input and 1 bar of inlet pressure) has been optimized in thrust, to evaluate the order of improvement using this optimization strategy.

The same CFD-optimization coupling method has been used as described previously in the nozzle simulations. The objective function is described by Eq.6, and the control variable is the nozzle half-angle α , with lower and upper bounds of 10-deg and 50-deg respectively.

$$J = (I_{sp} - \hat{I}_{sp})^2 \quad (6)$$

Figure 14 shows the Mach-number contours for two different nozzle angles, with same area ratio. On the left, the initial T50 nozzle with $\alpha = 14$ deg is represented, while on the right the optimized nozzle it is represented. As seen in the figure, the flow rapidly becomes supersonic and the viscous layers along the nozzle walls are very thick. The subsonic flow percentage of exit radius is 25.4% for $\alpha = 14$ deg, 28.2% for $\alpha = 26.7$ deg and 26.5% for the optimized nozzle, having for $\alpha_{opt} = 27.4$ deg. Even if the subsonic region of the first nozzle is slightly smaller than that one of the optimized angle, the former has a larger zone where the Mach number is below 3. Therefore, the 27.4-deg nozzle is shown to minimize the viscous effect. Additionally, it optimizes the thrust developed for the given inlet pressure and temperature, as a result of the trade-off with the divergence losses.

The results show an improvement in performance of about 2% in I_{sp} for the optimized 27.4 deg nozzle, increasing the specific impulse from 54 s to 55.07 s, and an improvement of thrust of about 2.5%. Performing the same optimization study for a turbulent flow case, e.g. 30 W of power and 2 bar of inlet pressure, gives $\alpha_{opt} = 15.5$ deg and a specific impulse improvement of only 10 ms. Kim² validated a similar CFD code with experimental results showing that for a low Reynolds number nozzle a contoured bell-shape nozzle has

the worst performance since it maximizes the viscous effect, a conclusion supported by this study. Whalen⁶ showed experimentally that the best low Reynolds number nozzle could have a trumpet geometry.

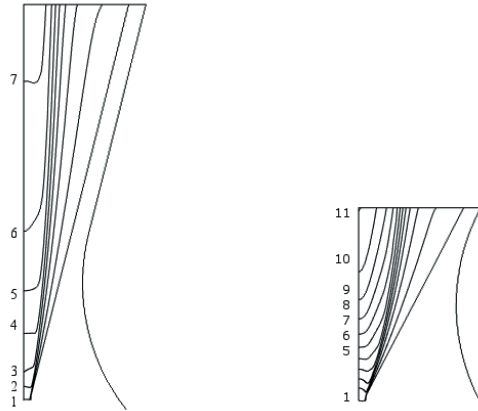


Figure 14. Mach number contours for initial ($\alpha = 14$ deg) and optimized ($\alpha = 27.4$ deg) nozzles

III. Future Work

A model for the SSTLs T50 heat exchanger is currently at a development stage, using Navier-Stokes equations coupled with heat transfer. The aim of this study is to deepen the knowledge of this device and heat transfer in resistojets, hence maximizing the performance of the 3000 K resistojet under study. The heat exchanger, shown in section view in Fig.3, cannot be modelled using axial symmetry, since the heating elements, two redundant wires, form an helical path around a bobbin, located upstream of the chamber and through which the propellant flows.

The 3D geometry has been constructed in SolidWorks and imported in COMSOL Multiphysics using a LiveLink node, which simplifies the complex 3D geometry management. To solve the problem, the Non-Isothermal Flow interface is used to couple heat transfer and Navier-Stokes equations. Joule heating is modelled using the Electrical Current interface, and the two interfaces are coupled in a temperature and a Heat Source node in the heater domains, defined as the total power dissipation density resulting from the Joule Heating. The heaters are modelled as four elements, two inner coils and two external coils. In the real thruster however, the heaters are two, since the inner and the outer coils are actually forming the same wire element. Figure 15, shows a view of the mesh utilised, where it is possible to distinguish between the inner Nichrome wire heaters and their Inconel sheath.

In the illustrated case, the inlet conditions are $\dot{m} = 20$ mg/s and $T_{in} = 293.15$ K. On the outlet is applied the total gas pressure $p_{out} = 2$ bar. Figure 16 shows a preliminary study output. The streamlines colour represent the stagnation temperature of the gas, that is heated from 300 K to a maximum temperature of 764 K. Finally, Fig.17 shows the temperature along the length of two heating elements. The inner heater temperature raises with approximately the same gradient as the longer outer heater, but reaching a lower final temperature, since its path length is shorter.

IV. Conclusions

Calculations are made on the SSTLs T50 Xenon resistojet nozzle. A CFD-optimization study was used to match the experimental measurements of specific impulse, thrust and nozzle surface temperature, based on a given inlet gas pressure and temperature from experimental measurements. Consequently, the model has been validated through a comparison between the numerical solution of the mass flow rate and its experimental value for the several experimental cases. In particular, the maximum relative error for mass flow rate was found to be 3.3%, with an average of 0.74%. The validated multiphysics computational model, gives the solution of the fully coupled compressible Navier-Stokes equations and heat transfer in both the gas and the nozzle wall domains. Among the full solution, they were analyzed in particular the nozzle radiation-

to-ambient loss, the inlet gas temperature of the gas and the Mach number iso-contours. The validated model has then been coupled with an optimization solver to study the effect of viscosity and divergence losses and to find the nozzle divergent section angle in order to maximize specific impulse, whilst maintaining the same inlet pressure and temperature. For the lower throat Reynolds number case, among the experimental data available, it was shown that the optimum nozzle angle is approximately double of the design one, improving the specific impulse by approximately 1 second. Finally, the future work on a multiphysics study on the T50 heat exchanger is illustrated. This CFD-optimization tool is now being used for the development of a next generation Very High Performance 3000 K Resistojet at the University of Southampton.

Acknowledgments

The University of Southampton would like to thank Surrey Satellite Technology Limited for providing extensive experimental data for use in the optimization study and for providing valuable insight on the construction and operation of the SSTL T-50 thruster. The authors acknowledge the use of the IRIDIS High Performance Computing Cluster and support services at the University of Southampton in completion of this work.

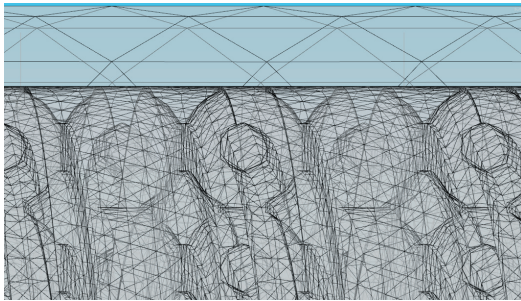


Figure 15. Detail on the T50 heat exchanger meshed domain

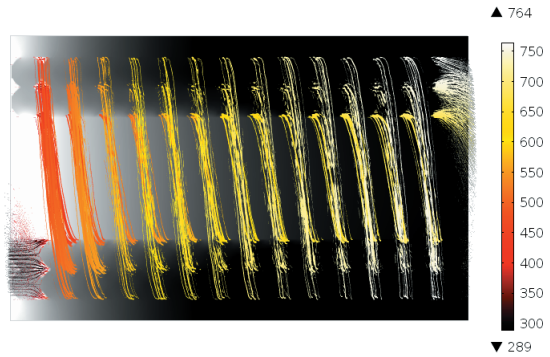


Figure 16. Stagnation temperature (K) of the Xenon gas streamlines

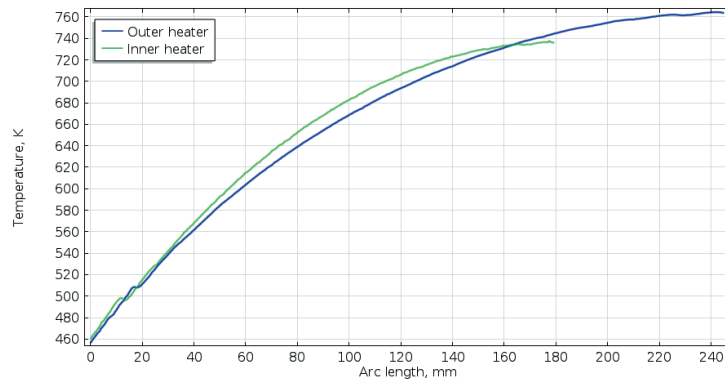


Figure 17. Temperature profiles evaluated along the heater coils length

References

- ¹Nicolini, D., Robertson, D., Chesta, E., Saccoccia, G., Gibbon, D., and Baker, A. "Xenon Resistojets as Secondary Propulsion on EP Spacecrafts and Performance Results of Resistojets using Xenon," IEPC-03-305
- ²Kim, S. C., "Calculations of Low-Reynolds-Number Resistojet Nozzles," *Journal of Spacecraft and Rockets*, Vol. 31, No. 2, 1994, pp. 259, 264.
- ³Bich, E., Millat, J., and Vogel, E., "The viscosity and thermal conductivity of pure monatomic gases from their normal boiling point up to 5000 K in the limit of zero density and at 0.101325 MP a," *J. Phys. Chem. Ref. Data*, , Vol. 19, No. 6, 1990, pp. 1289, 1305.
- ⁴Whalen, M. V., "Low Reynolds Number Nozzle Flow Study," *NASA Technical Memorandum*, 100130, 1987.
- ⁵Hussaini, M. M., and Korte, J. J., "Investigation of Low-Reynolds-Number Rocket Nozzle Design Using PNS-Based Optimization Procedure," *NASA Technical Memorandum*, 110295, 1996.
- ⁶Whalen, M. V., "Low Reynolds Number Nozzle Flow Study," *NASA Technical Memorandum*, 100130, 1987.
- ⁷COMSOL Multiphysics® Reference Manual, Software ver. 4.4, November 2013, COMSOL.